Biomaterials 291 (2022) 121873

Contents lists available at ScienceDirect

Biomaterials

journal homepage: www.elsevier.com/locate/biomaterials

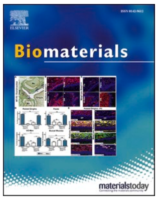

Orthogonal excitations of lanthanide nanoparticle up/down conversion emissions via switching NIR lights for in-vivo theranostics

Hongxia Zhao [a], Yuetong Li [a], Xiaobo Zhang [a], Kun Wu [a], Jiahang Lv [c], Cheng Chen [c], Huipu Liu [a], Zhuangzhi Shi [b,c], Huangxian Ju [a], Ying Liu [a,b,*]

[a] State Key Laboratory of Analytical Chemistry for Life Science, School of Chemistry and Chemical Engineering, Nanjing University, Nanjing 210023 China
[b] Chemistry and Biomedicine Innovation Center, Nanjing University, Nanjing 210023 China
[c] State Key Laboratory of Coordination Chemistry, School of Chemistry and Chemical Engineering, Nanjing University, Nanjing 210023 China

ARTICLE INFO

Keywords:
Lanthanide nanoparticle
Orthogonal up/down conversion luminescence
Activatable NIR-IIb imaging
In-vivo theranostics

ABSTRACT

With multiple emissions ranging from NIR-IIb to visible lights, near-infrared light-excited lanthanide nanoparticle (LnNP) is an ideal *in-vivo* theranostic platform to achieve imaging guided phototherapy. However, current reported LnNPs typically demonstrate simultaneous up and downconversion emissions with fixed single excitation light, which impairs therapeutic efficiency and generates side effect during navigation. Here we develop a lanthanide-based conversion switching nanoparticle (CSNP) with independent activation of 1550 nm NIR-IIb downconversion emission under 808 nm excitation and 345/450 nm upconversion emission under 980 nm excitation. CSNP is modified with Cy-GSH to quench NIR-IIb emission and photosensitizer hypocrellin A. *In vivo* delivery of CSNP is traced via 808 nm irradiation, and Cy-GSH changes structure in response to glutathione to activate NIR–IIb imaging. This indicates the tumor position and timing to switch for 980 nm irradiation to activate hypocrellin A for photodynamic therapy. Orthogonal activation of CSNP up/down conversion emissions demonstrates high tumor-to-normal tissue ratio *in vivo* and good therapeutic result, would have promising potential as a theranostics platform.

1. Introduction

In-vivo theranostics combines imaging and therapy into a single entity [1–3]. It offers prior diagnostic imaging on lesion areas, providing precise timing and location for the execution of therapy [4,5]. Second near-infrared (NIR-II) imaging at 1000–1700 nm offers deeper penetration and higher spatial resolution [6,7]. NIR-IIb (1500–1700 nm) is especially the gifted region with suppressed photon scattering [8–12]. Optical treatments, such as photodynamic therapy (PDT), rely on visible lights to perform non-invasive tumor killing [7,13–15]. Therefore, developing *in vivo* theranostics platform with on-demand activation of multi-luminance from NIR-IIb to visible region is very important.

By manipulating upconversion and downconversion energy transfer processes, near infrared (NIR) excited lanthanide-based nanoparticles (LnNPs) are capable of generating multiple emissions with narrow bandwidths in wide region from UV/visible to NIR-IIb [16,17]. This makes them appropriate materials for *in-vivo* theranostics. However, current reported up/down conversion LnNPs usually share single NIR excitation light and the same activator for both downconversion emission in NIR-IIb region and upconversion emission in UV/visible region [5,18,19], which results in the competitions of two energy transfer processes [18]. The lack of LnNPs luminescence control generates side effect during navigation process [20]. Techniques to improve NIR-IIb imaging quality are usually at the cost of suppressing upconversion luminescence, which impairs phototherapy efficiency and requires combined application with other therapeutic approaches to get satisfactory results [1,21–25]. An ideal *in-vivo* theranostics nanoplatform should have independent activations of NIR-IIb downconversion luminescence and UV/visible upconversion luminescence to achieve imaging guided precise execution of phototherapy. Approaches to orthogonally activating lanthanide nanoparticle up/down conversion emissions via switchable excitation lights are highly desired.

Though programmable activation of LnNPs multiple emissions have been achieved with different NIR excitations [20,26], the spectral manipulation is only limited in upconversion emission UV/visible region [27–34], rarely extended to downconversion emission NIR-IIb

---

[*] Corresponding author. State Key Laboratory of Analytical Chemistry for Life Science, School of Chemistry and Chemical Engineering, Nanjing University, Nanjing 210023 China.

E-mail address: yingliu@nju.edu.cn (Y. Liu).

https://doi.org/10.1016/j.biomaterials.2022.121873
Received 28 July 2022; Received in revised form 15 October 2022; Accepted 21 October 2022

region. Here we develop a lanthanide-based conversion switching nanoparticle (CSNP) with independent activations of downconversion NIR-IIb emission and upconversion UV/blue emission by switching 808/980 nm NIR irradiations, thus achieves *in-vivo* NIR-IIb imaging guided PDT. CSNP is composed of upconversion core $NaGdF_4$:Yb,Tm, downconversion zone $NaGdF_4$:Yb,Er,Ce@$NaYbF_4$:Nd, and inert layer $NaGdF_4$. Upconverion core generates upconversion emissions in UV/blue region at 345/450 nm upon 980 nm excitation, and downconverion zone generates downconversion emission in NIR-IIb region at 1550 nm upon 808 nm excitation (Scheme 1a). cRGD functionalized DSPE-PEG (DSPE-PEG-cRGD) and DSPE-PEG are modified on CSNPs surface to target cancer cells surface receptor $\alpha_v\beta_3$ integrin [35] and increase aqueous dispersion of nanoparticle. Cy-GSH, a non-emissive dye which recovers fluorescence in response to glutathione (GSH) is synthesized [36] and loaded on CSNPs surface via hydrophobic-hydrophobic interaction with DSPE. This endows CSNPs the capability of tumor cell activatable NIR-IIb imaging. Photosensitizer hypocrellin A (HA) is also loaded in CSNPs surface modified DSPE-PEG for ROS generation (Scheme 1b). The as-obtained CSNPs-Cy-GSH-HA-cRGD is intravenously injected to tumor bearing mice model and exposed under 808 nm excitation for imaging during systematic circulation process. Cy-GSH competes with CSNPs downconversion zone for absorbing 808 nm light energy, which suppresses CSNPs NIR-IIb emission and keeps it as "off" state during *in vivo* circulation (Scheme 1c, NIR-IIb "OFF"). Cy-GSH reacts with tumor cell over expressed GSH, and changes to F-SH that has intensive emission at 820 nm [36], which turns on CSNPs NIR-IIb luminance (Scheme 1c, NIR-IIb "ON"). This activatable NIR-IIb imaging yields a high tumor-to-normal tissue (T/N) ratio of 26.9, clearly indicating the location and timing to perform PDT. Subsequently the excitation light is switched to 980 nm, which activates CSNPs upconversion core for emission at 345–475 nm to generate ROS for PDT (Scheme 1c, NIR-IIb imaging-guided PDT), and results in prominent suppression for cell proliferation and tumor growth. This approach of orthogonally activating CSNPs NIR-IIb downconversion and upconversion luminance via switching NIR excitations would have promising potential in clinical application.

2. Experimental section

2.1. Materials

Rare-earth (III) anhydrous chloride (Yb, Gd, Nd, Ce, Tm, Er) were purchased from Alfa Asea and used as received. Sodium hydroxide (NaOH), ammonium fluoride (NH_4F), cyclohexene, 1-octadecene (ODE), oleic acid (OA), ethanol, chloroform, dimethyl sulfoxide (DMSO), dimethyl formamide (DMF),1,3-diphenylisobenzofuran (DPBF), 2,3,3-

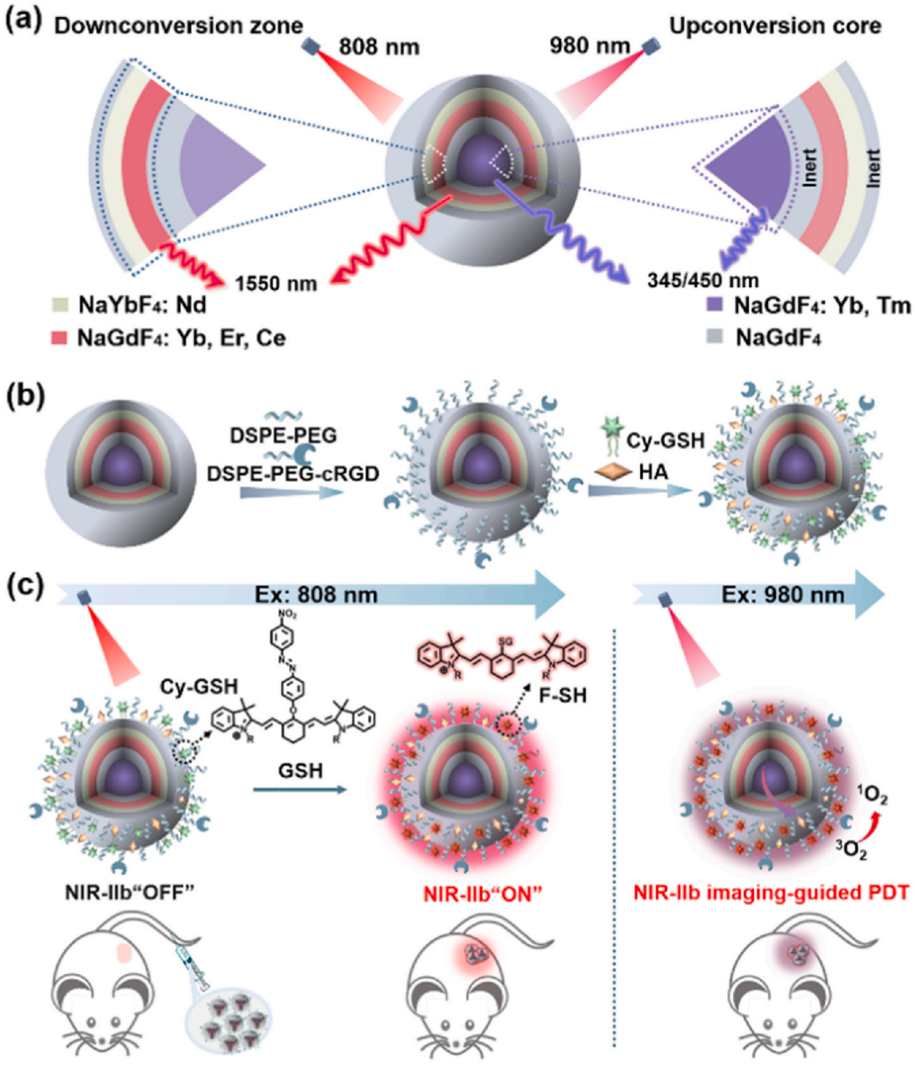

Scheme 1. Schematic illustration of orthogonal excitations of CSNPs up/down conversion emissions via due NIR lights for *in-vivo* theranostics. (a) CSNPs construction and up/down conversion emissions corresponding to dual NIR excitations. (b) Synthesis of CSNPs-Cy-GSH-HA-cRGD and (c) its application in activatable NIR-IIb imaging guided PDT.

Trimethylindolenine, 11-bromoundecanoic acid, acetonitrile, phosphorus oxychloride, cyclohexanone, 4-Nitroaniline, NaH, phenol, N-methylmaleimide (NMM), glutathione (GSH) were purchased from Aladin Ltd (Shanghai, China). Dichloromethane (CH_2Cl_2), trichloromethane ($CHCl_3$), methanol (MeOH), ethyl acetate and petroleum ether were supplied by Sinopharm Chemical Reagent Co., Ltd. (Shanghai, China). 1,2-distearoyl-*sn*-glycero-3-phosphoethanolamine-*N*-[methoxy (polyethylene glycol)] (DSPE-PEG, Mw = 2000) and cRGD functionalized DSPE-PEG (DSPE-PEG-cRGD) were purchased from Xi'an Rui Xi Biological Technology Co., Ltd. Hypocrellin A (HA) was purchased from Biopurify (Chengdu, China) Dulbecco's modified Eagle's medium (DMEM), 2′,7′ -dichlorofluorescein diacetate (DCFH-DA), medium3-(4,5-dimethylthiazol-2-yl)-2-diphenyltetrazolium (MTT) and annexin V-FITC apoptosis detection kit were purchased from Keygen Biotech (Nanjing, China). Fetal bovine serum (FBS) was purchased from (Thermo Fisher Scientific, USA). All chemicals were analytical grade and used without further purifications.

2.2. Apparatus

Transmission electron microscopic (TEM) images were acquired on JEM-2100 transmission electron microscope (JEOL Ltd., Japan). Powder X-ray diffraction (XRD) analysis was performed on ARL X'TRA XRD system (Thermo Fisher Scientific, USA). Dynamic light scattering (DLS) analysis was performed on ZetaPlus 90 Plus/BI-MAS (Brook haven, USA). Nuclear magnetic resonance (NMR) spectra were recorded on a Bruker DPX 400 MHz spectrometer. Ultraviolet visible-near infrared light (UV–Vis–NIR) absorption spectra were recorded with UV-3600 UV–vis–NIR spectrophotometer (Shimadzu Company, Japan). The cell images were captured on TCS SP5 confocal laser scanning microscope (CLSM) (Leica, Germany). MTT assays were conducted on Hitachi/Roche System Cobas 6000 (Bio-Rad, USA). Flow cytometric analysis was performed with CytoFLEX Flow Cytometer (Beckman-Coulter, USA). Upconversion luminescence (UCL) spectra and NIR-II fluorescence spectra were detected by a FL spectrometer F980 (Edinburgh Instruments, UK) under external 808 nm laser and 980 nm laser excitations. In vivo NIR-II fluorescence imaging was carried out by using NIR-II In Vivo Imaging System (Series III 900/1700, Suzhou NIR-Optics Technologies Co., Ltd., China) equipped with an 808-nm diode laser (100 mW/cm2) and 1350 nm long-pass (LP 1350) filter. In vitro NIR-II FL imaging was performed under a home-build microscope equipped with a 790 nm laser diode (Changchun New Industries Optoelectronics), a thermoelectric cooling two-dimensional InGaAs camera (NIRvana 640, 640 × 512 pixels; Princeton Instruments, detecting range 900–1700 nm), and 1350 nm long-pass filters (Thorlabs).

2.3. Synthesis of lanthanide-based conversion switching nanoparticle

2.3.1. Preparation of shell precursors for inert shell $NaGdF_4$ (S1, S4), and downconversion zone $NaGdF_4$:Yb,Er,Ce (S2), $NaYbF_4$:Nd (S3)

$GdCl_3$ (1.2 mmol) was mixed with 4 mL of OA and 12 mL of ODE, heated to 150 °C for 90 min in vacuum. The reaction solution was then cooled down to 45 °C. A solution of NaOH (3 mmol) and NH_4F (4.8 mmol) in methanol (12 mL) was added and the resultant mixture was stirred for half an hour. The reaction mixture was heated to 110 °C for 15 min to completely remove methanol and obtain inert shell precursor $NaGdF_4$ (S1, S4).

Downconversion zone shell precursors $NaGdF_4$:Yb,Er,Ce (S2) and $NaYbF_4$:Nd (S3) were prepared according to the above procedure with $YbCl_3$:$GdCl_3$:$ErCl_3$:$CeCl_3$ molar ratio of 40:18:2:40 and $YbCl_3$:$NdCl_3$ molar ratio of 50:50.

2.3.2. Synthesis of upconversion core $NaGdF_4$:Yb, 1%Tm

The synthesis of upconversion core was referred to our previous work [37]. $GdCl_3$ (0.5 mmol), $YbCl_3$ (0.49 mmol), and $TmCl_3$ (0.01 mmol) were mixed with 9 mL OA and 15 mL ODE, and stirred at 150 °C for 90 min under vacuum. After the solution was cooled down to 45 °C, 10 mL methanol solution containing 4 mmol NH_4F and 2.5 mmol NaOH was added dropwise and stirred at 45 °C for 30 min. Subsequently, methanol was removed by keeping the solution at 110 °C for 15 min and the reaction mixture was heated to 290 °C and kept for 90 min under nitrogen. After cooling down to room temperature, the nanoparticle products were centrifuged and washed twice with acetone and ethanol. The as-obtained upconversion core $NaGdF_4$:Yb, Tm was finally dispersed in 10 mL of cyclohexane for further use.

2.3.3. Synthesis of core-shell structured $NaGdF_4$:Yb,Tm@$NaGdF_4$ (CS_1)

Core-shell structured lanthanide-based nanoparticle was prepared with one-pot successive layer-by-layer (SLBL) protocol [38]. 2.85 mL of the above-obtained upconversion core $NaGdF_4$:Yb, Tm was mixed with 3.0 mL of OA and 9.0 mL of ODE. Cyclohexane was removed by keeping the solution at 85 °C for 30 min. The reaction mixture was then switched to N_2 flow and further heated to 300 °C. Subsequently, 4 mL of the above prepared inert shell precursor $NaGdF_4$ (S1, 1.2 mmol) was injected into the reaction mixture and kept at 300 °C for 30 min for the shell growth. The above shell coating step was repeated 2 times to get a satisfactory thickness of S1. The as-obtained $NaGdF_4$:Yb,Tm@$NaGdF_4$ (CS1) was precipitated and washed with acetone and ethanol and re-dispersed in cyclohexane for future use.

2.3.4. Synthesis of core-shell structured $NaGdF_4$:Yb, Tm@$NaGdF_4$@$NaGdF_4$:Yb,Er,Ce (CS2)

The above-obtained CS1 was mixed with 3.0 mL of OA and 9.0 mL of ODE, kept at 85 °C for 30 min, and heated to 300 °C in N_2 flow. 4 mL of the above prepared down conversion zone shell precursor $NaGdF_4$:Yb, Er,Ce (S2, 1.0 mmol) was injected into the reaction mixture and kept at 300 °C for 30 min to grow the first layer of down conversion zone. The above shell coating step was repeated 2 times to get a satisfactory thickness of S2. $NaGdF_4$:Yb,Tm@$NaGdF_4$@$NaGdF_4$:Yb,Er,Ce (CS2) was precipitated with acetone, washed twice with acetone and ethanol, and re-dispersed in cyclohexane for future use.

2.3.5. Synthesis of core-shell structured $NaGdF_4$:Yb, Tm@$NaGdF_4$@$NaGdF_4$:Yb,Er,Ce@$NaYbF_4$:Nd (CS3)

The above-obtained CS2 was mixed with 3.0 mL of OA and 9.0 mL of ODE, kept at 85 °C for 30 min, and heated to 300 °C in N_2 flow. 8 mL of the above prepared down conversion zone shell precursor $NaYbF_4$:Nd (S3, 1.0 mmol) was injected into the reaction mixture and kept at 300 °C for 30 min to grow the second layer of down conversion zone. The above shell coating step was repeated 2 times to get a satisfactory thickness of S3. The as-obtained $NaGdF_4$:Yb,Tm@$NaGdF_4$@$NaGdF_4$:Yb,Er,Ce@NaGdF4:Nd (CS3) was precipitated with acetone, washed twice with acetone and ethanol, and re-dispersed in cyclohexane for future use.

2.3.6. Synthesis of $NaGdF_4$:Yb,Tm@$NaGdF_4$@$NaGdF_4$:Yb,Er, Ce@$NaYbF_4$:Nd@$NaGdF_4$ (CSNPs)

The above-obtained CS3 was mixed with 3.0 mL of OA and 9.0 mL of ODE, kept at 85 °C for 30 min, and heated to 300 °C in N_2 flow. 4 mL of the above prepared inert shell precursor $NaGdF_4$ (S4, 1.0 mmol) was injected into the reaction mixture and kept at 300 °C for 30 min to complete the synthesis of $NaGdF_4$:Yb,Tm@$NaGdF_4$@$NaGdF_4$:Yb,Er, Ce@$NaGdF_4$:Nd@$NaGdF_4$ (CSNPs). The as obtained CSNPs were precipitated with acetone, washed twice with acetone and ethanol, and re-dispersed in cyclohexane for future use.

2.4. Preparation of Cy-GSH functionalized CSNPs (CSNPs-Cy-GSH)

10 mg of the above-obtained CSNPs and 10 mg amphiphilic polymer DSPE-PEG were dispersed in chloroform, mixed in a 10 mL flask, and continuously stirred overnight. Chloroform solvent was then slowly evaporated under nitrogen atmosphere. The residue was dispersed in ultrapure water with 5 min ultra-sonication. The as-obtained PEG

functionalized CSNPs were centrifuged, washed with ultrapure water three times, and dispersed into HEPES buffer (pH 7.2) for future use.

Cy-GSH was synthesized according to a previously reported approach [36]. ^{1}H NMR (400 MHz, DMSO-d_6) δ 8.43 (d, J = 9.0 Hz, 2H), 8.08 (dd, J = 17.3, 8.8 Hz, 4H), 7.80 (d, J = 14.1 Hz, 2H), 7.51 (d, J = 7.4 Hz, 2H), 7.45 (d, J = 8.6 Hz, 2H), 7.38 (d, J = 7.0 Hz, 4H), 7.20 (td, J = 7.1, 1.7 Hz, 2H), 6.25 (d, J = 14.2 Hz, 2H), 4.16 (d, J = 7.6 Hz, 4H), 3.99 (t, J = 6.6 Hz, 4H), 2.77 (t, J = 6.1 Hz, 4H), 2.26 (t, J = 7.3 Hz, 4H), 1.92 (s, 2H), 1.70 (s, 4H), 1.51 (dd, J = 10.0, 8.0, 5.2 Hz, 8H), 1.31 (d, J = 7.5 Hz, 24H), 1.23 (s, 16H), 0.87 (s, 6H) (Fig. S1). ^{13}CNMR (101 MHz, DMSO) δ 173.37, 172.17, 163.04, 161.79, 155.53, 148.77, 147.63, 142.47, 141.38, 140.64, 128.99, 126.51, 125.57, 125.42, 123.85, 122.93, 121.37, 116.13, 111.82, 101.02, 63.78, 49.13, 49.02, 44.07, 33.97, 30.68, 29.23, 29.20, 29.07, 28.88, 27.63, 27.27, 26.45, 24.93, 24.18, 21.10, 19.09, 13.99 (Fig. S2). HPLC-MS (m/z): [M]+ calculated for $[C_{72}H_{96}N_5O_7]^+$ 1142.73, found 1142.65 (Fig. S3).

Cy-GSH was dissolved in DMSO, and slowly added into PEG functionalized CSNPs dispersed HEPES buffer (100 mM, pH 7.2). The mixture was kept shaking overnight to load Cy-GSH into DSPE-PEG layer, and subsequently centrifuged to remove the excess Cy-GSH. The as-obtained CSNPs-Cy-GSH was washed with ultrapure water and redispersed in water to a final concentration of 1 mg/mL. The loading concentration of Cy-GSH was optimized to get the maximum suppress of CSNPs luminance in 1550 nm.

2.5. *Preparation of Cy-GSH/HA/targeting molecule cRGD functionalized CSNPs (CSNPs-Cy-GSH-HA-cRGD)*

HA was dissolved in DMSO, mixed with 1 mg of above-obtained CSNPs-Cy-GSH in 1 mL water, and stirred overnight in dark. The product was centrifuged, washed with ultrapure water, and the as-obtained CSNPs-Cy-GSH-HA-cRGD was re-dispersed in PBS for future use. The loading concentration of HA was optimized to get the efficient generation of ROS.

To endow CSNPs tumor cell targeting capability, CSNPs-Cy-GSH-HA-cRGD was prepared by using DSPE-PEG/DSPE-PEG-cRGD (mass ratio = 90:10, in total 10 mg) mixture instead of DSPE-PEG in the first surface modification step, and the as-obtained CSNPs-PEG-cRGD was continuously functionalized according to the same procedure as described above.

2.6. *In vitro response of CSNPs-Cy-GSH-HA-cRGD to GSH*

1 mg/mL CSNPs-Cy-GSH-HA-cRGD dispersed HEPES buffer (pH 7.2) was mixed with various concentrations of GSH, respectively. The mixtures were incubated at 37 °C for 10 min. NIR-II fluorescence spectra were measured subsequently with a continuous wave laser excitation at 808 nm and a power density of about 1 W/cm^2.

To verify the reaction selectivity of CSNPs-Cy-GSH-HA-cRGD to GSH, 1 mg/mL CSNPs-Cy-GSH-HA-cRGD dispersed HEPES buffer (pH 7.2) was mixed with 10 mM interfering substance Ala, Thr, Val, Asn, Phe, Glu, Cys, Lys, His, Ser, Pro, $MgCl_2$, KCl, NaCl, Glucose and GSH, respectively. The mixtures were incubated at 37 °C for 1 h, and NIR-II fluorescence spectra were measured according to the same procedure above.

2.7. *Stability of CSNPs-Cy-GSH-HA-cRGD*

To study thermal stability, 1 mg/mL CSNPs-Cy-GSH-HA-cRGD were dispersed in PBS (pH 7.4), incubated at 37 °C, and NIR-II fluorescence spectra were measured at different intervals time. To study pH stability, 1 mg/mL CSNPs-Cy-GSH-HA-cRGD were dispersed in PBS with different pH, incubated at 37 °C for 1 h, and NIR-II fluorescence spectra were measured at different intervals time. In addition, the hydration size of CSNPs-Cy-GSH-HA-cRGD was also monitored during 72 h incubation in PBS, saline, and DMEM containing 10% FBS.

2.8. *Cell culture*

MDA-MB-231 and MCF-10A cells were cultured in DMEM cell culture medium complemented with 10% FBS, streptomycin (100 mg/mL) and penicillin (100 mg/mL) at 37 °C in a humidified atmosphere containing 5% CO_2. Cell numbers were counted by a Petroff-Hausser cell counter (USA).

2.9. *In vitro ROS generation*

1 mL CSNPs-Cy-GSH-HA-cRGD dispersed ethanol solution (5 mg/mL) was mixed with 20 μL DPBF ethanol solution (2.5 mg/mL), and irradiated with a 980 nm laser at 1 W/cm^2 for 70 min. DPBF absorbance was monitored at 412 nm from supernatant every 10 min.

The intracellular ROS generation was measured by incubating MDA-MB-231 cells with 200 μg/mL CSNPs-Cy-GSH-HA-cRGD for 4 h and 50 μM DCFH-DA diacetate for 30 min at 37 °C. The treated cells were then exposed under 980 nm laser at 1 W/cm^2 for 30 min (with 5 min break after each 10 min exposure) to take the CLSM fluorescence images. Control experiments were also performed for CSNPs-Cy-GSH-HA-cRGD treated MDA-MB-231 cells in the absence of NIR irradiation and under 808 nm laser irradiation.

2.10. *Mitochondrial membrane assay*

MDA-MB-231 cells (2 × 10^5 per well) were seeded into a 12-well plate and incubated with CSNPs-Cy-GSH-HA or CSNPs-Cy-GSH-HA-cRGD (200 μg/mL) in the cell incubator for 4 h, respectively, irradiated with 980 nm laser at 1 W/cm^2 for 30 min (with 5 min break after each 10 min exposure), and continuously incubated for 12 h. MDA-MB-231 cells treated with PBS in the absence of NIR irradiation were tested as controls. The cells were then collected and washed twice with PBS, 0.5 mL of freshly prepared JC-1 working solution was added and incubated in a CO_2 incubator at 37 °C for 10–15 min. After incubation, cells were washed twice with 1X assay buffer and then centrifuged for 5 min at 2000 rpm. After centrifugation, cells were resuspended in 0.5 mL of 1X assay buffer and analyzed by flow cytometry.

2.11. *NIR-IIb imaging of MDA-MB-231 and MCF-10A cells*

MDA-MB-231 or MCF-10A cells were rinsed with PBS thrice, incubated with 200 μg/mL CSNPs-Cy-GSH-HA-cRGD in DMEM under 5% CO_2 at 37 °C for 4 h, respectively. The cells were rinsed with PBS thrice and imaged in the region of 1400–1700 nm under 790 nm laser excitation. For negative control experiments, MDA-MB-231 cells were pretreated with 1, 3 and 5 mM NMM for 0.5 h to suppress the intracellular GSH expression, incubated with CSNPs-Cy-GSH-HA-cRGD and imaged under the same conditions.

2.12. *Cell cytotoxicity*

The cytotoxicity of CSNPs-PEG-cRGD, CSNPs-Cy-GSH-HA-cRGD and NMM to MDA-MB-231 cells was evaluated by MTT assay. MDA-MB-231 cells were cultured in a 96-well plate (1 × 10^4 per well) for 24 h. The cell culture medium was then replaced with fresh DMEM containing serial concentrations of CSNPs-PEG-cRGD, CSNPs-Cy-GSH-HA-cRGD (0, 25, 50, 100, 200, 400 μg/mL) and NMM (5 mM), respectively, and continuously incubated for 24 h. Subsequently, 20 μL of 0.5 mg/mL MTT solution was added into each well. After additional incubation of 4 h, the medium was carefully aspirated and replaced with 150 μL of DMSO. After brief shaking for 15 min, the absorbance was measured with Bio-Rad microplate reader at 490 nm. The relative cell viability was calculated using the following equation: cell viability rate (%) = $OD_{treatment}/OD_{control} \times 100\%$.

To evaluate the therapeutic effect of CSNPs-Cy-GSH-HA-cRGD to MDA-MB-231 cells. The cells were treated with different concentrations of CSNPs-Cy-GSH-HA-cRGD for 4 h, washed with PBS two times, and exposed under 980 nm light with a power density of 1 W/cm^2 for 30 min (with 5 min break after each 10 min exposure). The above treated cells were then continuously cultured for 24 h to analyze the cell viability with MTT assay. The same treated MDA-MB-231 cells were exposed under 808 nm laser or in the absence of NIR irradiation as controls.

2.13. Cell apoptosis assay

MDA-MB-231 cells (2x10^5 per well) were seeded into a 12-well plate and incubated with CSNPs-Cy-GSH-HA-cRGD (200 μg/mL) in the cell incubator for 4 h, irradiated with 980 nm laser at 1 W/cm^2 for 30 min (with 5 min break after each 10 min exposure) and continuously incubated for 28 h. The same treated MDA-MB-231 cells under 808 nm laser irradiation or in the absence of NIR irradiation were also tested as controls. The cells were then collected and washed with PBS thrice, stained with the mixture of 5.0 μL Annexin V-FITC and 5.0 μL propidium iodide for 15 min, and measured with flow cytometry.

2.14. In vivo NIR-II imaging

BALB/c Nude mice bearing orthotopic breast cancer tumor were purchased from GemPharmatech (Nanjing, China), and all procedures were performed in accordance with the NIH guidelines for the care and use of laboratory animals (NIH Publication no. 85-23 Rev. 1985) and approved by the Animal Ethical and Welfare Committee of Nanjing University with approval No of IACUC-2202004. The tumor-bearing mice for NIR-IIb imaging were randomly divided into three groups (n = 3): (i) "always-on'' nanoprobe CSNPs-PEG-cRGD (2 mg/mL, 200 μL) injected group, (ii) CSNPs-Cy-GSH-HA-cRGD (2 mg/mL, 200 μL) injected group, and (iii) CSNPs-Cy-GSH-HA-cRGD injected group with GSH expression inhibited. Mice in GSH inhibited group were injected with 200 μL NMM (1 mg/kg) and incubated for 1 h to suppress GSH expression. Healthy mice were also injected with CSNPs-Cy-GSH-HA-cRGD as (iv) control group (n = 3). The mice were imaged at different time points post injection, and 2 L/min oxygen flow with 1.5% isoflurane was used for mice anesthesia during injection and imaging.

2.15. In vivo photodynamic therapy (PDT) effect

The tumor-bearing mice for *in vivo* PDT were randomly divided into four groups (n = 3): (i) saline injected group, (ii) CSNPs-Cy-GSH-HA-cRGD (2 mg/mL, 200 μL) injected group that in the absence of NIR irradiation (iii) CSNPs-Cy-GSH-HA-cRGD (2 mg/mL, 200 μL) injected group under 808 nm laser irradiation, and (iv) CSNPs-Cy-GSH-HA-cRGD (2 mg/mL, 200 μL) injected group under 980 nm laser irradiation. When NIR-IIb imaging reached maximum intensity under 808 nm irradiation, the irradiation light was switched to therapeutic irradiation to perform PDT. Groups (iii) and (iv) were irradiated with 808 nm and 980 nm (1 W/cm^2) respectively for 30 min (5 min break for each 10 min exposure). The laser exposure was repeated at day 3 and day 6, and the tumor volumes along with the weight of the mice were recorded every 2 days. All the animals were sacrificed at day 14. The tumor volumes were calculated as $V = (L \times W^2)/2$, where L and W are the length and width of the tumor, respectively. The tumor and major organs including heart, spleen, kidney, liver, and lung were harvest for the histopathological analysis. The organs were fixed with 4% paraformaldehyde, embedded in paraffin blocks, sliced to sections with 5 μm thickness, and stained with hematoxylin and eosin for histopathological analysis.

2.16. In vivo circulation and excretion of nanoprobe

Healthy BALB/c nude mice (n = 3) were intravenously injected with "always-on" nanoprobe CSNPs-PEG-cRGD (2 mg/mL, 200 μL) to study its *in vivo* circulation and excretion. The mice were imaged under 808 nm to monitor the circulation of CSNPs-PEG-cRGD for 24 h. Mice feces were collected at predetermined time points during a period of 6 days. The major organs of mice were collected at day 6, weighted and dissolved in 2 mL nitric acid at 70 °C for 12 h. Each sample was diluted with deionized water and the corresponding Gd^{3+} concentration was determined by ICP-AES.

3. Results and discussion

3.1. Design and characterization of conversion switching nanoparticles (CSNPs)

$NaGdF_4$:Yb,Tm@$NaGdF_4$@$NaGdF_4$:Yb,Er,Ce@$NaYbF_4$:Nd@$NaGdF_4$ (CSNPs) was composed of upconversion core, downconversion zone, and inert layer (Scheme 1a). The upconversion core $NaGdF_4$:Yb, Tm has β-$NaGdF_4$ crystalline structure co-doped with Yb^{3+} and Tm^{3+} with diameter of 14.4 ± 0.48 nm (Fig. 1a, core). The upconversion core was coated with $NaGdF_4$ inert shell (S1) to prevent energy transfer and restrain cross-relaxation between upconversion core and downconversion zone [28]. The as-obtained core-shell structured nanoparticle $NaGdF_4$:Yb,Tm@$NaGdF_4$ (CS1) demonstrated diameter of 23.5 ± 1.01 nm (Fig. 1a, CS1). The downconversion zone contained two shells, $NaGdF_4$:Yb,Er, Ce for NIR-IIb emission (S2), which increased particle diameter to 30.5 ± 0.85 nm (Fig. 1a, CS2), and $NaYbF_4$:Nd for NIR excitation lights absorption (S3), which increased particle diameter to 32.5 ± 1.05 nm (Fig. 1a, CS3). Another inert shell of $NaGdF_4$ (S4) was subsequently grown on CS3 to eliminate the surface-related quenching of luminescence, and completed CSNPs with particle diameter of 36.3 ± 0.77 nm (Fig. 1a, CS4). Upconversion core and all the core-shell structured nanoparticles demonstrated uniform sizes (Fig. 1a, Fig. S4a). X-ray diffraction (XRD) patterns of CSNPs showed a highly crystalline hexagonal phase consistent with β-$NaGdF_4$ standard pattern (JCPDS: 27–0699) (Fig. S4b). The distribution of lanthanide ions in different layers of CSNPs was confirmed by energy dispersive spectroscopy (EDS) mapping, which indicated the continuous distribution of Yb^{3+}, Gd^{3+} over multi-layers, as well as the distributions of Ce^{3+} and Nd^{3+} in outer shells (Fig. S4c).

Orthogonal excitation of CSNPs downconversion and upconversion luminances via alternate 980/808 nm excitations were achieved by separating lanthanide activator Er^{3+} and Tm^{3+} in different shells of CSNPs and manipulating corresponding energy transfer. Nd^{3+} in S3 of downconversion zone harvested photons from 808 nm light. The absorbed excitation light energy migrated over Yb sublattice through interionic cross-relaxation, and finally entrapped by activator Er^{3+} (2%) embedded in S2 to generate NIR-II emission at 1550 nm due to non-radiative relax from $^4I_{11/2} \rightarrow {}^4I_{13/2}$ state and continuous radiative relax to $^4I_{15/2}$ state [39]. Ce^{3+} (40%) was co-doped in S2, which accelerated non-radiative relax from $^4I_{11/2} \rightarrow {}^4I_{13/2}$, thereby boosted the downconversion luminance of Er^{3+} and suppressed its upconversion emission at 550 nm ($^4S_{3/2} \rightarrow {}^4I_{15/2}$) and 650 nm ($^4F_{9/2} \rightarrow {}^4I_{15/2}$) [18] (Fig. 1b and c). The thickness of S2 was also optimized as 3.5 nm to achieve high NIR-II emission intensity. Sensitizer Yb^{3+} in upconversion core absorbed energy from 980 nm excitation, which was then transferred to activator Tm^{3+} through classical energy upconversion transfer process and generated UV/Vis emission at 345 and 365 nm corresponding to $^1I_6 \rightarrow {}^3F_4$ and $^1D_2 \rightarrow {}^3H_6$ transitions, and at 455 and 475 nm corresponding to $^1D_2 \rightarrow {}^3F_4$ and $^1G_4 \rightarrow {}^3H_6$ transitions [40] (Fig. 1b and c, 980 nm). Inert shell $NaGdF_4$ (S1) with thickness of 4.5 nm successfully inhibited energy transfer from Yb^{3+} in the S2 layer to Tm^{3+} in upconversion core, which prevented upconversion emission from 808 nm excitation (Fig. 1c, 808 nm). Downconversion luminance peaks were also observed at 1550 nm and 1475 nm under 980 nm excitation, which were corresponding to energy transition from Yb^{3+} to Er^{3+} in S2 and Yb^{3+} to Tm^{3+} ($^3H_4 \rightarrow {}^3F_4$) in core respectively (Fig. 1c, 980 nm).

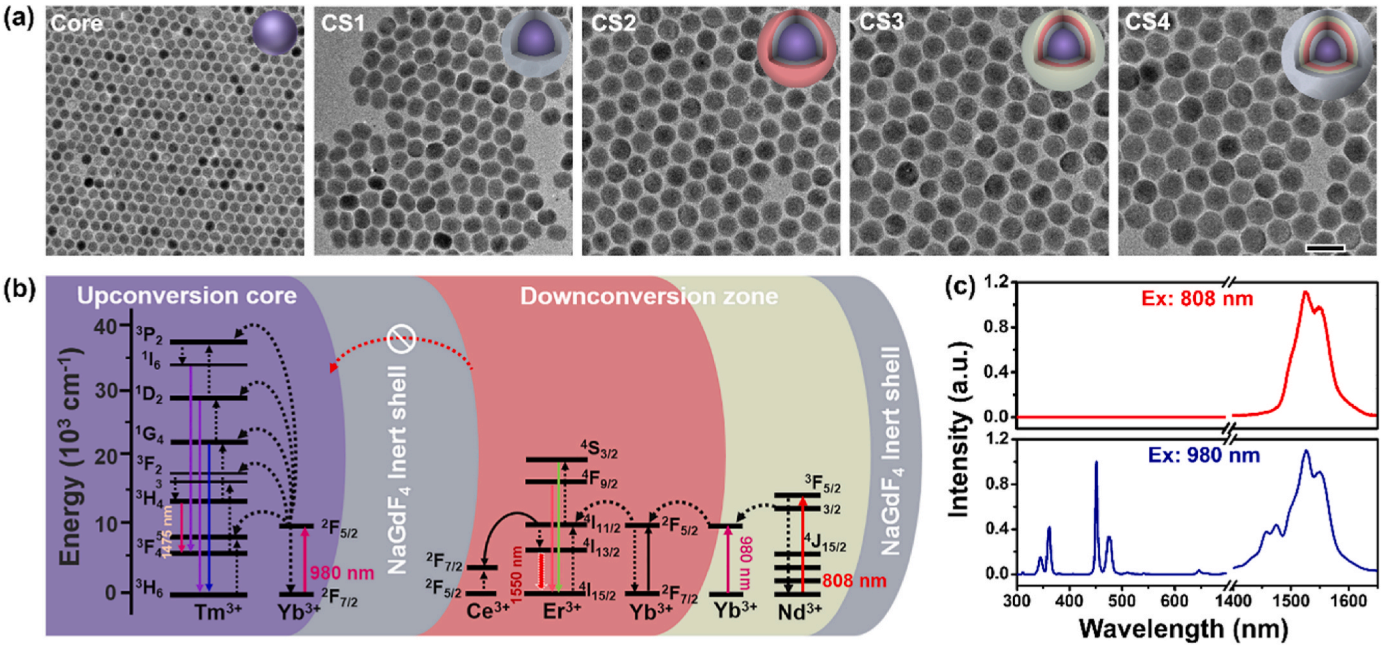

Fig. 1. Characterizations of CSNPs up/down conversion emissions. (a) TEM images of upconversion core and layered structure CS1, CS2, CS3, CS4 (CSNPs. Scale bars are 50 nm). (b) Energy-transfer mechanisms and (c) luminance spectra of CSNPs under 808 nm and 980 nm irradiations.

3.2. Synthesis and characterization of CSNPs-Cy-GSH-HA-cRGD

Cy-GSH, which converts structure in response to GSH, was synthesized according to a previously reported approach [36], and acted as cancer cells indicator dye. Cy-GSH presented strong absorption around 808 nm (Fig. 2a, Cy-GSH absorption) with molar absorption coefficients 10^4 times that of Nd^{3+}, but no emission due to intramolecular photo induced electron transfer (PET) [36] (Fig. 2a, Cy-GSH emission). Reacting with GSH invalidated the intramolecular PET process, therefor the product F-SH showed strongly enhanced emission at 820 nm with unchanged absorption peak (Fig. 2a, F-SH emission and absorption). The large emission difference in 820 nm for Cy-GSH in response to GSH makes it an appropriate switcher molecule for CSNPs activatable NIR-IIb emission. CSNPs with oleic acid (OA) as surface ligand was modified with amphiphilic polymer DSPE-PEG. Hydrophobic DSPE was immobilized on CSNPs surface via hydrophobic-hydrophobic interaction with OA, and hydrophilic PEG was stretched out to extend system circulation [41].

The as-obtained PEG functionalized CSNPs demonstrated DSPE-PEG characteristic peaks at 1730 cm^{-1} in Fourier transform infrared (FTIR) spectrum corresponding to C=O stretching of ester groups (Fig. S5a). TEM image also showed a uniform coating layer on CSNPs with DSPE-PEG modification (Fig. S5b). Cy-GSH was loaded in the hydrophobic cavity formed between ligand OA and DSPE, and the as-obtained CSNPs-Cy-GSH demonstrated Cy-GSH characteristic absorption peaks at 790 nm and 342 nm (Fig. 2b, CSNPs-Cy-GSH). Cy-GSH competed with Nd^{3+} for absorbing 808 nm excitation light, and demonstrated concentration dependent suppression of CSNPs NIR-IIb emission under 808 nm excitation (Fig. S5c). After reacting with GSH, Cy-GSH was converted to F-SH, whose emission matched well with Nd^{3+} absorption (Fig. 2a). Therefore, F-SH acted as antenna molecule to improve 808 nm light absorption and amplify NIR-IIb emission under 808 nm excitation [36], which exceeded the NIR-IIb emission intensity under 980 nm excitation (Fig. S5d). The enhancement effect was affected by the loading amount of Cy-GSH on CSNPs surface, and it even suppressed NIR-IIb emission with loading concentration above 50 μmol/mg due to ACQ effect [42] (Fig. S5d). The emission intensity of CSNPs-Cy-GSH at 1550 nm after GSH reaction was higher than that before GSH reaction, and achieved 25 μmol/mg as the optimal concentration of Cy-GSH loading on CSNPs (Fig. S5e). The loading of Cy-GSH increased the hydrodynamic diameter of PEG functionalized CSNPs from 41.34 ± 4.46 to 59.68 ± 4.26 nm and zeta potential from −1.09 ± 0.18 to 2.55 ± 0.29 mV due to the positive charge of Cy-GSH (Fig. 2c).

Photosensitizer HA, with its maximum absorption overlapped with CSNPs upconversion emission peak at 450 and 475 nm under 980 nm excitation (Fig. S6a), was subsequently loaded on CSNPs-Cy-GSH surface via hydrophobic-hydrophobic interaction with DSPE. The as-obtained CSNPs-Cy-GSH-HA demonstrated decreased intensity for upconversion emission peaks at 345/365 nm and 455/475 nm, indicating the successful loading of HA on CSNPs surface (Fig. S6b). CSNPs-Cy-GSH-HA with different HA loading concentrations all demonstrated complete suppression for 1550 nm NIR-IIb luminance under 808 nm excitation (Fig. S7a) with efficient recovery in response to GSH (Fig. S7b). The recovered NIR-IIb luminance intensity was slightly decreased with higher HA loading concentrations (Fig. S7b). The effect of HA loading concentration on ROS generation efficiency was evaluated by 1,3-diphenylisobenzofuran (DPBF), which reacts with ROS and decreases characteristic absorbance at 410 nm [43]. DPBF characteristic absorbance continuously decreased according to time under 980 nm irradiation for all CSNPs-Cy-GSH-HA with different HA loading concentrations (Fig. S7c). The loading concentration of HA on CSNPs-Cy-GSH was optimized by evaluating ROS generation efficiency and NIR-IIb luminance intensity, and 50 μmol/mg was determined as the optimal loading concentration (Fig. S7d). The as-obtained CSNPs-Cy-GSH-HA showed a series of HA characteristic absorption peaks at 472, 541, and 583 nm (Fig. 2b, CSNPs-Cy-GSH-HA), and increased hydrodynamic diameter to 63.29 ± 6.60 nm and zeta potential to 2.95 ± 0.27 mV (Fig. 2c).

To facilitate tumor cell targeting, DSPE-PEG-cRGD, which specifically targets $\alpha_v\beta_3$ integrin overexpressed on tumor cell membrane [35], was mixed with DSPE-PEG in surface modification step. The as-obtained CSNPs-Cy-GSH-HA-cRGD showed sphere shape (Fig. 2d) with hydrodynamic diameter of 69.29 ± 3.12 nm and zeta potential of 3.73 ± 0.32 mV (Fig. 2c). Under 808 nm excitation, CSNPs-Cy-GSH-HA-cRGD barely showed NIR-IIb downconversion emission in the absence of GSH (Fig. 2e, inset, GSH(−)), and the NIR-IIb downconversion emission increased according to GSH concentration (Fig. 2e). In response to 10 mM GSH, as the common GSH concentration in tumor cells [44,45],

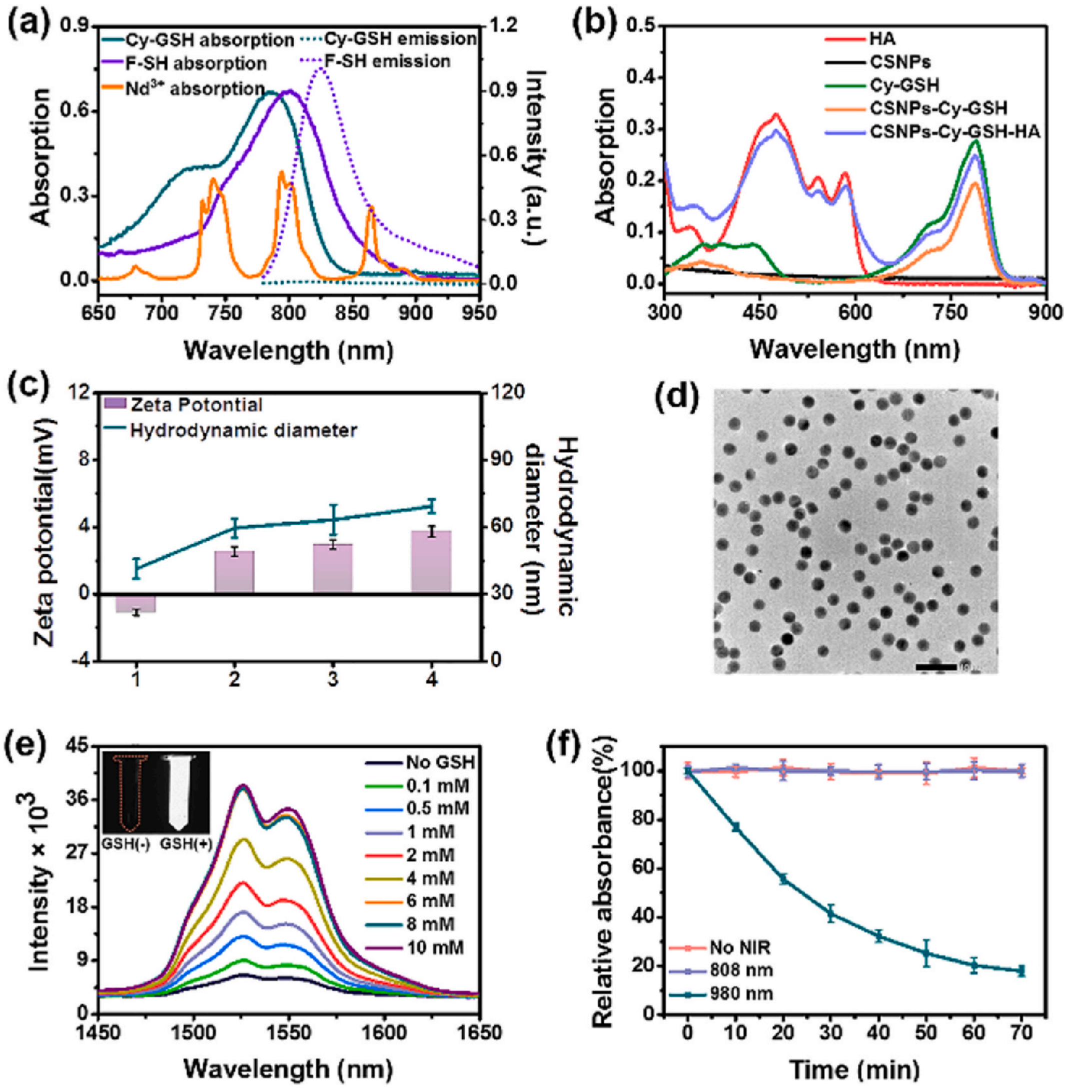

Fig. 2. Characterizations of CSNPs surface functionalization process. (a) Absorption spectra of Cy-GSH, F-SH, Nd^{3+} and emission spectra of Cy-GSH and F-SH. (b) Absorption spectra of HA, CSNPs, Cy-GSH, CSNPs-Cy-GSH, and CSNPs-Cy-GSH-HA. (c) Hydrodynamic diameter and zeta potential of (1) PEG functionalized CSNPs, (2) CSNPs–Cy-GSH, (3) CSNPs–Cy-GSH-HA, and (4) CSNPs-Cy-GSH-HA-cRGD. (d) TEM image of CSNPs-Cy-GSH-HA-cRGD. Scale bar indicates 100 nm. (e) NIR-II luminance spectra of CSNPs-Cy-GSH-HA-cRGD under 808 nm excitation in response to GSH (0.1–10 mM). (f) Time dependent relative absorption percentages of DPBF at 410 nm for CSNPs-Cy-GSH-HA-cRGD under 980 nm, 808 nm excitations and in the absence of NIR excitation. The error bars indicate means ± S.D. (n = 3).

CSNPs-Cy-GSH-HA-cRGD demonstrated bright NIR-IIb fluorescence (Fig. 2e, inset, GSH(+)), indicating the efficient tumor cell activatable NIR-IIb emission. The fluorescence intensity was similar to CSNP-HA-cRGD and CSNPs-Cy-GSH-HA-cRGD under 980 nm excitation, probably because the co-immobilized HA affected reaction efficiency of Cy-GSH with GSH (Fig. S8). To further evaluate the response specificity of CSNPs-Cy-GSH-HA-cRGD to GSH, it was challenged with usual ions and molecules, which barely demonstrated NIR-IIb emission recovery (Fig. S9a). Downconversion NIR-IIb luminance of CSNPs-Cy-GSH-HA-cRGD and its response to GSH remained stable at different pH (Fig. S9b) and during 24 h incubation at 37 °C (Fig. S9c). Under 980 nm excitation, the upconversion emission of CSNPs-Cy-GSH-HA-cRGD at 450 and 475 nm activated HA for ROS generation, and demonstrated time dependent decrease of DPBF characteristic absorbance at 410 nm (Fig. S10a, Fig. 2f, 980 nm). CSNPs-Cy-GSH-HA-cRGD demonstrated similar decrease percentage of DPBF absorption peak in 70 min compared with that of CSNPs-Cy-GSH-HA (Fig. S7c), indicating that cRGD didn't affect ROS generation efficiency. There was no DPBF characteristic absorption peak decrease observed under 808 nm excitation (Figs. 2f, 808 nm), demonstrating the good manipulation of ROS generation with excitation light switching. CSNPs-Cy-GSH-HA-cRGD showed stable size in PBS, saline and cell culture medium DMEM + FBS(10%) without obvious aggregation (Fig. S10b).

3.3. Orthogonal activation of cellular NIR-IIb imaging and PDT via 808/980 nm excitation lights switching

Breast cancer cell MDA-MB-231 was chosen as the model cell to verify the capability of CSNPs-Cy-GSH-HA-cRGD for sequential activating NIR-IIb imaging and therapy. CSNPs-Cy-GSH-HA-cRGD treated MDA-MB-231 cells demonstrated obvious intracellular distribution of nanoparticles in bio-TEM (Fig. S11), indicating efficient endocytosis of CSNPs-Cy-GSH-HA-cRGD.

The feasibility of CSNPs-Cy-GSH-HA-cRGD for activatable NIR-IIb imaging of tumor cells was verified under 808 nm excitation, which demonstrated intense intracellular luminance in the long-wavelength region (1400–1700 nm) (Fig. 3a, No NMM). NIR-IIb fluorescence signal was barely observed from CSNPs-Cy-GSH-HA-cRGD incubated normal MCF-10A cells due to the low expression of $\alpha_v\beta_3$ integrin at cell

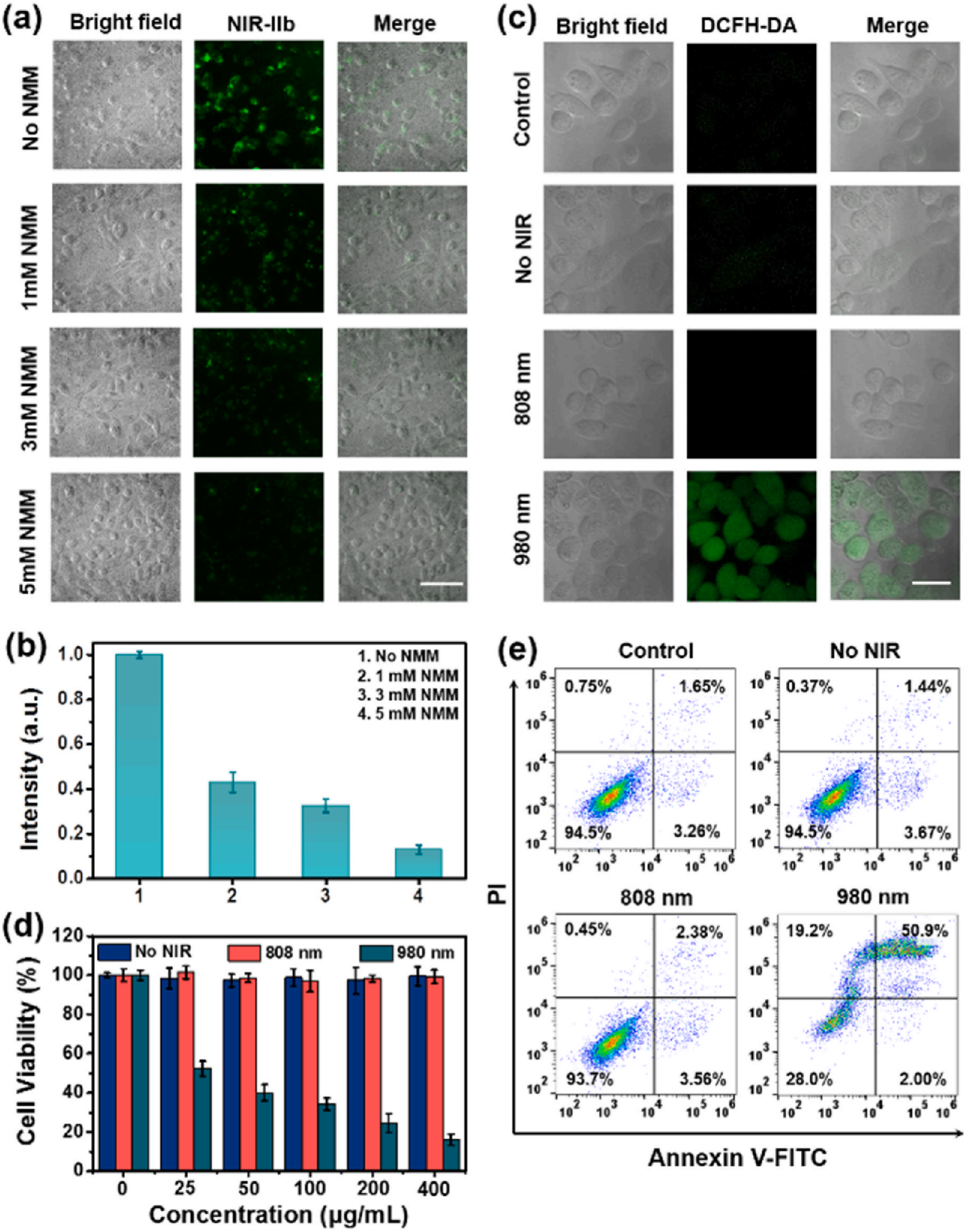

Fig. 3. Activation of cellular NIR-IIb imaging and PDT via 808/980 nm excitation lights switching. (a) NIR-IIb fluorescence images of CSNPs-Cy-GSH-HA-cRGD incubated MDA-MB-231 cells (No NMM), and MDA-MB-231 cells that pretreated with 1 mM, 3 mM, 5 mM NMM under 808 nm excitation, scale bar: 100 μm, and (b) its corresponding intensity collected in 1400–1700 nm region. (c) Confocal microscopic images of CSNPs-Cy-GSH-HA-cRGD incubated MDA-MB-231 cells under 980 nm irradiation, 808 nm irradiation, and in the absence of NIR irradiation (No NIR) then stained with DCFH-DA. Scale bar: 50 μm. (d) Cell viability of various concentrations CSNPs-Cy-GSH-HA-cRGD (0–400 μg/mL) treated MDA-MB-231 cells under 980 nm, 808 nm excitations and in the absence of NIR irradiation. (e) Flow cytometric analysis of untreated MDA-MB-231 cells (control) and MDA-MB-231 cells incubated with 200 μg/mL CSNPs-Cy-GSH-HA-cRGD under 980 nm, 808 nm excitations and in the absence of NIR irradiation. The error bars indicate means ± S.D. (n = 3).

membrane and low expression of intracellular GSH (Fig. S12). To further show GSH expression dependent NIR-IIb luminance intensity, MDA-MB-231 cells were pretreated with *N*-methylmaleimide (NMM) that suppresses intracellular GSH [46]. NMM pretreatment barely affected cell viability (Fig. S13). NMM pretreated MDA-MB-231 cells demonstrated decreased NIR-IIb luminance corresponding to NMM concentrations (Fig. 3a and b 1,3,5 mM NMM). Upon switching excitation light from 808 nm to 980 nm, ROS production in MDA-MB-231 cells was investigated with 2′,7′ -dichlorofluorescein diacetate (DCFH-DA) as detection probe. CSNPs-Cy-GSH-HA-cRGD incubated MDA-MB-231 cells demonstrated bright intracellular fluorescence under 980 nm excitation, indicating efficient ROS generation (Figs. 3c, 980 nm). On the contrary, DCFH-DA fluorescence was barely observed from the same treated MDA-MB-231 cells under 808 nm excitation (Figs. 3c, 808 nm), similar to the situations of CSNPs-Cy-GSH-HA-cRGD incubated MDA-MB-231 cells in the absence of NIR irradiation (Fig. 3c, No NIR). The independent manipulation of ROS generation with dual NIR excitation lights guarantees the sequential activations of NIR-IIb imaging and PDT. CSNPs-Cy-GSH-HA-cRGD and CSNPs-PEG-cRGD demonstrated good biocompatibility of with little effect on MDA-MB-231 cells viability in the absence of NIR irradiation (Fig. 3d, No NIR, Fig. S13). Under 980 nm excitation, the cell viability was gradually decreased with CSNPs-Cy-GSH-HA-cRGD concentration increase, and reached 16.2% for 400 μg/mL CSNPs-Cy-GSH-HA-cRGD incubated MDA-MB-231 cell (Figs. 3d, 980 nm). 808 nm irradiation had little effect on cell viability (Figs. 3d, 808 nm). Flow cytometry assay using the Annexin V-fluorescein isothiocyanate (FITC)/PI apoptotic kit showed similar result. 200 μg/mL CSNPs-Cy-GSH-HA-cRGD did not induce apoptosis of MDA-MB-231 cells in the absence of NIR irradiation or under 808 nm excitation (Fig. 3e, No NIR, 808 nm). 980 nm irradiation caused 72.1% of cells in apoptosis and even cell necrosis (Figs. 3e, 980nm). This result further confirmed that the separation of navigation and photo-therapy excitation lights could avoid side effect and guarantee efficient therapy. JC-1 assay was performed to verify the specific therapeutic effect of CSNPs-Cy-GSH-HA-cRGD. It demonstrated much lower red fluorescence with higher depolarization of mitochondrial membrane potential for CSNPs-Cy-GSH-HA-cRGD treated MDA-MB-231 cells compared with CSNPs-Cy-GSH-HA treated MDA-MB-231 cells (Fig. S14).

3.4. *Activatable NIR-IIb imaging guided PDT in vivo*

CSNPs-PEG-cRGD, which has “always on” NIR-IIb luminance in the absence of Cy-GSH and no toxicity in the absence of HA, was prepared and intravenously injected into healthy mice to evaluate the biocompatibility of nanoprobe, as well as its *in vivo* distribution and excretion. NIR-IIb imaging at 1550 nm provided deeper tissue penetration, therefore the major organs and multistage blood vessels of mice were clearly visible within 4 h of injection (Fig. S15a). NIR-IIb fluorescence signal in liver gradually increased in 9 h after injection, and kept decreased until barely observed after 4 days (Fig. S15a and Fig. S15b). Organ distribution results also demonstrated high NIR-IIb fluorescence in liver and spleen at 9 h post-injection, with little retention in other organs including heart, lung, kidney (Fig. S16). And about 78.9% of the injected CSNPs-PEG-cRGD excreted in feces at 6 days post-injection measured by ICP-MS (Fig. S17a) with very little amount remained in main organs at 6th day (Fig. S17b), indicating a rapid biliary excretion pathway. The hematoxylin and eosin (H&E) staining results of the major organs including heart, liver, spleen, lung, and kidney demonstrated little damage (Fig. S18), further confirmed good biocompatibility of CSNPs-PEG-cRGD.

The sequential activations of CSNPs up/down conversion for activatable NIR-IIb imaging guided cancer therapy was evaluated with orthotopic MDA-MB-231 breast cancer mice model. CSNPs-Cy-GSH-HA-cRGD was intravenously injected into the tumor bearing mice, which started to show NIR-IIb downconversion emission at tumor grown site at 10 min post-injection under 808 nm excitation. NIR-IIb fluorescence intensity increased with time, and reached maximum at 4 h post-injection (Fig. 4a, Tumor mice, CSNPs-Cy-GSH-HA-cRGD), precisely indicating the time to switch for upconversion emission with 980 nm excitation to perform phototherapy. Activatable NIR-IIb luminance signal was observed in tumor grown area due to the high expression level of GSH in tumor cells, which clearly indicate the position to perform 980 nm irradiation for PDT. NIR-II luminescence signal was also observed in liver considering the higher concentration of GSH in liver than in blood vessels [45,47]. CSNPs-Cy-GSH-HA-cRGD also demonstrated similar NIR-IIb fluorescence intensity throughout the mice body under 980 nm excitation (Fig. S19). In comparison, “always on” NIR-IIb nanoprobe CSNPs-PEG-cRGD demonstrated extensively distributed NIR-IIb signal throughout the mice body (Fig. 4a, Tumor mice, CSNPs-PEG-cRGD). It was not until 4 h post-injection that tumor grown site showed distinguishable NIR-IIb fluorescence intensity from background, but the borders between tumors and normal tissues were still too fuzzy to tell apart. CSNPs-PEG-cRGD also showed higher NIR-IIb fluorescence intensity in liver compared with activatable probe CSNPs-Cy-GSH-HA-cRGD, since CSNPs-Cy-GSH-HA-cRGD was not fully activated by GSH in liver position. Organ distribution results also demonstrated high NIR-IIb fluorescence intensity from CSNPs-PEG-cRGD in liver, spleen and tumor grown position at 4 h post-injection with little retention in other organs (Fig. S20). To further verify the activation of NIR-IIb fluorescence by GSH in tumor cell, tumor bearing mice were pretreated with NMM to suppress GSH expression and intravenously injected with CSNPs-Cy-GSH-HA-cRGD, it demonstrated very weak NIR-IIb fluorescence at tumor grown position under 808 nm excitation (Fig. 4a, Tumor mice, CSNPs-Cy-GSH-HA-cRGD + NMM). Healthy mice group that injected with CSNPs-Cy-GSH-HA-cRGD didn't show *in vivo* NIR-IIb fluorescence either (Fig. 4a, Healthy mice, CSNPs-Cy-GSH-HA-cRGD). Numbers 1,2,3 were assigned for the tumor region, tissue adjacent to tumor, and background respectively. The tumor-to-normal tissue (T/N) ratios were calculated according to time following the equation: [(mean fluorescence intensity of 1) - (mean fluorescence intensity of 3)]/[(mean fluorescence intensity of 2) - (mean fluorescence intensity of 3)]. It reached 26.9 for CSNPs-Cy-GSH-HA-cRGD injected mice group and only 0.72 for CSNPs-PEG-cRGD injected mice group at 4 h (Fig. 4b, 4hr). The activatable NIR-IIb imaging resulted in high T/N ratio, which identified the location of lesion areas sharply and indicated the precise location and optimal timing to perform therapy.

With the precise navigation of activatable downconversion NIR-IIb imaging, 4 h post intravenous injection was chosen as the time point for switching excitation light from 808 nm to 980 nm to perform PDT. The activatable NIR-IIb imaging guided PDT resulted in satisfactory inhibition on tumor growth for CSNPs-Cy-GSH-HA-cRGD injected tumor bearing mice under 980 nm irradiation, while the CSNPs-Cy-GSH-HA-cRGD injected tumor bearing mice in the absence of NIR irradiation or CSNPs-Cy-GSH-HA-cRGD injected tumor bearing mice under 808 nm irradiation showed a continuous increase of tumor volume similar to saline-treated tumor bearing mice group (Fig. 4c). Photographs of tumor-bearing mice also demonstrated strongest inhibition of tumor growth with CSNPs-Cy-GSH-HA-cRGD injection under 980 nm exposure (Fig. S21). There was no discernible decrease in body weight observed for all experiment groups (Fig. 4d). The successful tumor growth inhibition was further confirmed by H&E and TUNEL, which showed highest level of apoptosis or necrosis for tumor cells from CSNPs-Cy-GSH-HA-cRGD treated mice group under 980 nm irradiation (Fig. 4e). Major organs (heart, liver, spleen, lung, and kidney) showed no obvious damage or significant abnormalities for all treated mice via H&E staining (Fig. S22). These results showed the sequential activation of downconversion and upconversion of CSNPs for NIR-IIb imaging-guiding precision phototherapy, which would have potential advantages in imaging navigated tumor therapy.

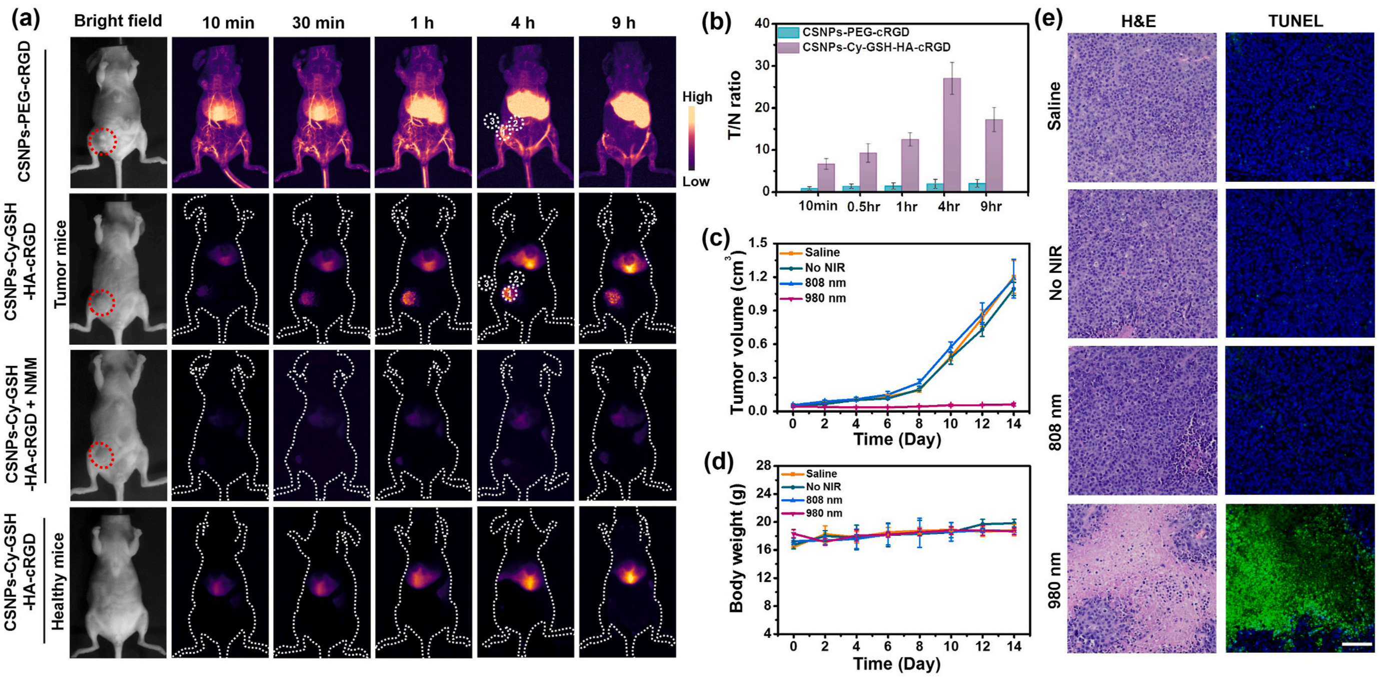

Fig. 4. Activatable NIR-IIb imaging guided PDT *in vivo*. (a) Timespan of NIR-IIb fluorescence imaging in MDA-MB-231 tumor bearing mice after injection of CSNPs-Cy-GSH-HA-cRGD, CSNPs-PEG-cRGD, NMM pretreated tumor bearing mice after injection of CSNPs-Cy-GSH-HA-cRGD (CSNPs-Cy-GSH-HA-cRGD + NMM), and healthy mice after injection of CSNPs-Cy-GSH-HA-cRGD under 808 nm irradiation, and (b) corresponding tumor-to-normal tissue (T/N) ratios for tumor bearing mice injected with CSNPs-Cy-GSH-HA-cRGD or CSNPs-PEG-cRGD. Error bars indicated means ± SD (n = 3). (c) Relative tumor growth, (d) body weight and (e) histological observations of tumor tissues stained with H&E and TUNEL for tumor bearing mice injected with saline, CSNPs-Cy-GSH-HA-cRGD in the absence of NIR irradiation (No NIR), under 808 nm irradiation (808 nm) and 980 nm irradiation (980 nm). Scale bar in (e): 100 μm. Error bars in (b), (c), (d) indicate means ± SD (n = 3).

4. Conclusion

In conclusion, CSNPs with orthogonally regulated 1550 nm NIR-IIb downconversion emission and 345/450 nm UV/blue upconversion emission by switching 808/980 nm excitations was presented in this manuscript. CSNPs were also modified with Cy-GSH for tumor cell activatable NIR-IIb imaging, and HA for PDT. The activatable NIR-IIb imaging under 808 nm irradiation yielded a high T/N ratio, which clearly indicated the timing to switch for 980 nm irradiation and position of tumor grown to perform PDT. Both *in vitro* and *in vivo* experiments showed prominent suppression for cell proliferation and tumor growth. The CSNPs with orthogonally regulated downconversion/upconversion emissions via switching dual NIR excitations would have promising potential in NIR-IIb imaging navigated tumor therapy.

Credit author statement

Ying Liu conceived, designed the experiments, and supervise the project. Hongxia Zhao, Yue Li, Xiaobo Zhang, Kun Wu, Jiahang Lv, Cheng Chen and Huipu Liu performed the experiments. Hongxia Zhao, Huangxian Ju, Zhuangzhi Shi and Ying Liu analyzed the data. Hongxia Zhao and Ying Liu wrote the manuscript.

Declaration of competing interest

The authors declare that they have no known competing financial interests or personal relationships that could have appeared to influence the work reported in this paper.

Data availability

Data will be made available on request.

Acknowledgments

We gratefully acknowledge the National Natural Science Foundation of China (22022405, 21974064), Natural Science Foundation of Jiangsu Province for distinguished Young Scholars (BK20200010).

Appendix A. Supplementary data

Supplementary data to this article can be found online at https://doi.org/10.1016/j.biomaterials.2022.121873.

References

[1] J. Xu, R. Shi, G. Chen, S. Dong, P. Yang, Z. Zhang, N. Niu, S. Gai, F. He, Y. Fu, J. Lin, All-in-One theranostic nanomedicine with ultrabright second near-infrared emission for tumor-modulated bioimaging and chemodynamic/photodynamic therapy, ACS Nano 14 (8) (2020) 9613–9625.

[2] C. Wang, W.P. Fan, Z.J. Zhang, Y. Wen, L. Xiong, X.Y. Chen, Advanced nanotechnology leading the way to multimodal imaging-guided precision surgical therapy, Adv. Mater. 31 (49) (2019), 1904329.

[3] Y. Cai, X.Y. Chen, J.X. Si, X.Z. Mou, X.C. Dong, All-in-One nanomedicine: multifunctional single-component nanoparticles for cancer theranostics, Small 17 (52) (2021), 2103072.

[4] M. Tang, X.H. Zhu, Y.H. Zhang, Z.P. Zhang, Z.M. Zhang, Q.S. Mei, J. Zhang, M. H. Wu, J.L. Liu, Y. Zhang, Near-infrared excited orthogonal emissive upconversion nanoparticles for imaging-guided on-demand therapy, ACS Nano 13 (9) (2019) 10405–10418.

[5] Y. Zhong, Z. Ma, F. Wang, X. Wang, Y. Yang, Y. Liu, X. Zhao, J. Li, H. Du, M. Zhang, Q. Cui, S. Zhu, Q. Sun, H. Wan, Y. Tian, Q. Liu, W. Wang, K.C. Garcia, H. Dai, In vivo molecular imaging for immunotherapy using ultra-bright near-infrared-IIb rare-earth nanoparticles, Nat. Biotechnol. 37 (11) (2019) 1322–1331.

[6] G. Hong, A.L. Antaris, H. Dai, Near-infrared fluorophores for biomedical imaging, Nat. Biomed. Eng. 1 (1) (2017), 0010.

[7] C. Li, G. Chen, Y. Zhang, F. Wu, Q. Wang, Advanced fluorescence imaging technology in the near-infrared-II window for biomedical applications, J. Am. Chem. Soc. 142 (35) (2020) 14789–14804.

[8] C.Y. Li, Q.B. Wang, Challenges and opportunities for intravital near-infrared fluorescence imaging technology in the second transparency window, ACS Nano 12 (10) (2018) 9654–9659.

[9] Z. Feng, T. Tang, T.X. Wu, X.M. Yu, Y.H. Zhang, M. Wang, J.Y. Zheng, Y.Y. Ying, S. Y. Chen, J. Zhou, X.X. Fan, S.L. Li, M.X. Zhang, J. Qian, Perfecting and extending the near-infrared imaging window, Light Sci. Appl. 10 (1) (2021) 197.

[10] N.N. Zhang, C.Y. Lu, M.J. Chen, X.L. Xu, G.F. Shu, Y.Z. Du, J.S. Ji, Recent advances in near-infrared II imaging technology for biological detection, J. Nanobiotechnol. 19 (1) (2021) 132.

[11] F.F. Wang, F.Q. Ren, Z.R. Ma, L.Q. Qu, R. Gourgues, C. Xu, A. Baghdasaryan, J. C. Li, I.E. Zadeh, J.W.N. Los, A. Fognini, J. Qin-Dregely, H.J. Dai, In vivo non-invasive confocal fluorescence imaging beyond 1,700 nm using superconducting nanowire single-photon detectors, Nat. Nanotechnol. (2022), https://doi.org/10.1038/s41565-022-01130-3.

[12] F.F. Wang, L.Q. Qu, F.Q. Ren, A. Baghdasaryan, Y.Y. Jiang, R. Hsu, P. Liang, J.C. Li, G.Z. Zhu, Z.R. Ma, H.J. Dai, High-precision tumor resection down to few-cell level guided by NIR-IIb molecular fluorescence imaging, Proc. Natl. Acad. Sci. U.S.A. 119 (15) (2022), e2123111119.

[13] S. Gao, G. Wei, S. Zhang, B. Zheng, J. Xu, G. Chen, M. Li, S. Song, W. Fu, Z. Xiao, W. Lu, Albumin tailoring fluorescence and photothermal conversion effect of near-infrared-II fluorophore with aggregation-induced emission characteristics, Nat. Commun. 10 (1) (2019) 2206.

[14] H.X. Lin, Z.X. Lin, K.H. Zheng, C.L. Wang, L.S. Lin, J.X. Chen, J.B. Song, Near-infrared-II nanomaterials for fluorescence imaging and photodynamic therapy, Adv. Opt. Mater. 9 (9) (2021), 2002177.

[15] S.Q. He, J. Song, J.L. Qu, Z. Cheng, Crucial breakthrough of second near-infrared biological window fluorophores: design and synthesis toward multimodal imaging and theranostics, Chem. Soc. Rev. 47 (12) (2018) 4258–4278.

[16] Z.G. Yi, Z.C. Luo, X. Qin, Q.S. Chen, X.G. Liu, Lanthanide-activated nanoparticles: a toolbox for bioimaging, therapeutics, and neuromodulation, Acc. Chem. Res. 53 (11) (2020) 2692–2704.

[17] J. Xu, A. Gulzar, P. Yang, H. Bi, D. Yang, S. Gai, F. He, J. Lin, B. Xing, D. Jin, Recent advances in near-infrared emitting lanthanide-doped nanoconstructs: mechanism, design and application for bioimaging, Coord. Chem. Rev. 381 (2019) 104–134.

[18] Y. Zhong, Z. Ma, S. Zhu, J. Yue, M. Zhang, A.L. Antaris, J. Yuan, R. Cui, H. Wan, Y. Zhou, W. Wang, N.F. Huang, J. Luo, Z. Hu, H. Dai, Boosting the down-shifting luminescence of rare-earth nanocrystals for biological imaging beyond 1500 nm, Nat. Commun. 8 (1) (2017) 737.

[19] C. Cao, N. Wu, W. Yuan, Y.Y. Gu, J.M. Ke, W. Feng, F.Y. Li, Ln(3+)-doped nanoparticles with enhanced NIR-II luminescence for lighting up blood vessels in mice, Nanoscale 12 (15) (2020) 8248–8254.

[20] Z. Zhang, Y. Zhang, Orthogonal emissive upconversion nanoparticles: material design and applications, Small 17 (11) (2021), 2004552.

[21] L. Li, B. Zhang, Y. Liu, R. Gao, J. Zhou, L.M. Fu, J. Wang, A spontaneous membrane-adsorption approach to enhancing second near-infrared deep-imaging-guided intracranial tumor therapy, ACS Nano 15 (3) (2021) 4518–4533.

[22] X. Li, M. Jiang, S. Zeng, H. Liu, Polydopamine coated multifunctional lanthanide theranostic agent for vascular malformation and tumor vessel imaging beyond 1500 nm and imaging-guided photothermal therapy, Theranostics 9 (13) (2019) 3866–3878.

[23] H.R. Chen, F.X. Wu, X.Y. Xie, W. Wang, Q.Q. Li, L.P. Tu, B. Li, X.G. Kong, Y. L. Chang, Hybrid nanoplatform: enabling a precise antitumor strategy via dual-modal imaging-guided photodynamic/chemo-/immunosynergistic therapy, ACS Nano 15 (12) (2021) 20643–20655.

[24] Z. Liu, B.F. Yun, Y.B. Han, Z.L. Jiang, H.Q. Zhu, F. Ren, Z. Li, Dye-sensitized rare earth nanoparticles with up/down conversion luminescence for on-demand gas therapy of glioblastoma guided by NIR-II fluorescence imaging, Adv. Healthcare Mater. 11 (3) (2022), 2102042.

[25] Q.X. Wang, Y.F. Yang, X.F. Yang, Y. Pan, L.D. Sun, W.Y. Zhang, Y. Shao, J. Shen, J. Lin, L. Li, C.H. Yan, Upconverted/downshifted NaLnF4 and metal-organic framework heterostructures boosting NIR-II imaging-guided photodynamic immunotherapy toward tumors, Nano Today 43 (2022), 101439.

[26] H. Dong, L.D. Sun, W. Feng, Y.Y. Gu, F.Y. Li, C.H. Yan, Versatile spectral and lifetime multiplexing nanoplatform with excitation orthogonalized upconversion luminescence, ACS Nano 11 (3) (2017) 3289–3297.

[27] K.Z. Zheng, S.Y. Han, X. Zeng, Y.M. Wu, S.Y. Song, H.J. Zhang, X.G. Liu, Rewritable optical memory through high-registry orthogonal upconversion, Adv. Mater. 30 (30) (2018), 1801726.

[28] X.M. Li, Z.Z. Guo, T.C. Zhao, Y. Lu, L. Zhou, D.Y. Zhao, F. Zhang, Filtration shell mediated power density independent orthogonal excitations-emissions upconversion luminescence, Angew. Chem. Int. Ed. 55 (7) (2016) 2464–2469.

[29] J.P. Lai, Y.X. Zhang, N. Pasquale, K.B. Lee, An upconversion nanoparticle with orthogonal emissions using dual NIR excitations for controlled two-way photoswitching, Angew. Chem. Int. Ed. 53 (52) (2014) 14419–14423.

[30] M. Wu, L. Yan, T. Wang, B. Zhou, Q.Y. Zhang, Controlling red color-based multicolor upconversion through selective photon blocking, Adv. Funct. Mater. 29 (25) (2019), 1804160.

[31] X. Liu, H.M. Chen, Y.T. Wang, Y.G. Si, H.X. Zhang, X.M. Li, Z.C. Zhang, B.A. Yan, S. Jiang, F. Wang, S.J. Weng, W.D. Xu, D.Y. Zhao, J.Y. Zhang, F. Zhang, Near-infrared manipulation of multiple neuronal populations via trichromatic upconversion, Nat. Commun. 12 (1) (2021) 5662.

[32] Q.S. Mei, A. Bansal, M.K.G. Jayakumar, Z.M. Zhang, J. Zhang, H. Huang, D.J. Yu, C.J.A. Ramachandra, D.J. Hausenloy, T.W. Soong, Y. Zhang, Manipulating energy migration within single lanthanide activator for switchable upconversion emissions towards bidirectional photoactivation, Nat. Commun. 10 (2019) 4116.

[33] Z.H. Di, B. Liu, J. Zhao, Z.J. Gu, Y.L. Zhao, L.L. Li, An orthogonally regulatable DNA nanodevice for spatiotemporally controlled biorecognition and tumor treatment, Sci. Adv. 6 (25) (2020), eaba9381.

[34] Y. Yang, J. Huang, W. Wei, Q. Zeng, X. Li, D. Xing, B. Zhou, T. Zhang, Switching the NIR upconversion of nanoparticles for the orthogonal activation of photoacoustic imaging and phototherapy, Nat. Commun. 13 (1) (2022) 3149.

[35] A. Srivatsan, M. Ethirajan, S.K. Pandey, S. Dubey, X. Zheng, T.H. Liu, M. Shibata, J. Missert, J. Morgan, R.K. Pandey, Conjugation of cRGD peptide to chlorophyll a based photosensitizer (HPPH) alters its pharmacokinetics with enhanced tumor-imaging and photosensitizing (PDT) efficacy, Mol. Pharm. 8 (4) (2011) 1186–1197.

[36] T. Liang, Z. Li, P.P. Wang, F.Z. Zhao, J.Z. Liu, Z.H. Liu, Breaking through the signal-to-background limit of upconversion nanoprobes using a target-modulated sensitizing switch, J. Am. Chem. Soc. 140 (44) (2018) 14696–14703.

[37] X.B. Zhang, W.W. Chen, X.Y. Xie, Y.Y. Li, D.S. Chen, Z.C. Chao, C.H. Liu, H.B. Ma, Y. Liu, H.X. Ju, Boosting luminance energy transfer efficiency in upconversion nanoparticles with an energy-concentrating zone, Angew. Chem. Int. Ed. 58 (35) (2019) 12117–12122.

[38] X.M. Li, D.K. Shen, J.P. Yang, C. Yao, R.C. Che, F. Zhang, D.Y. Zhao, Successive layer-by-layer strategy for multi-shell epitaxial growth: shell thickness and doping position dependence in upconverting optical properties, Chem. Mater. 25 (1) (2013) 106–112.

[39] B. Huang, Y.X. Zhou, F.J. Yang, L.B. Wu, Y.W. Qi, J. Li, The 1.53 mu m spectroscopic properties of Er3+/Ce3+/Yb3+ tri-doped tellurite glasses containing silver nanoparticles, Opt. Mater. 51 (2016) 9–17.

[40] Y.J. Liu, Y.Q. Lu, X.S. Yang, X.L. Zheng, S.H. Wen, F. Wang, X. Vidal, J.B. Zhao, D. M. Liu, Z.G. Zhou, C.S. Ma, J.J. Zhou, J.A. Piper, P. Xi, D.Y. Jin, Amplified stimulated emission in upconversion nanoparticles for super-resolution nanoscopy, Nature 543 (7644) (2017) 229–233.

[41] M. Zhang, Z.J. Wang, C.X. Wang, Y.T. Wu, Z. Li, Z.H. Liu, Visualizing oxidative stress level for timely assessment of ischemic stroke via a ratiometric near-infrared-II luminescent nanoprobe, ACS Nano 15 (7) (2021) 11940–11952.

[42] T. Liang, Q.R. Wang, Z. Li, P.P. Wang, J.J. Wu, M.M. Zuo, Z.H. Liu, Removing the obstacle of dye-sensitized upconversion luminescence in aqueous phase to achieve high-contrast deep imaging in vivo, Adv. Funct. Mater. 30 (16) (2020), 1910765.

[43] Y.Y. Li, X.B. Zhang, Y. Zhang, Y.L. He, Y. Liu, H.X. Ju, Activatable photodynamic therapy with therapeutic effect prediction based on a self-correction upconversion nanoprobe, ACS Appl. Mater. Interfaces 12 (17) (2020) 19313–19323.

[44] C.L. Wang, H.X. Lin, X.G. Ge, J. Mu, L.C. Su, X. Zhang, M. Niu, H.H. Yang, J. B. Song, Dye-sensitized downconversion nanoprobes with emission beyond 1500 nm for ratiometric visualization of cancer redox state, Adv. Funct. Mater. 31 (16) (2021), 2009942.

[45] X.Y. Jiang, B.J. Du, J. Zheng, Glutathione-mediated biotransformation in the liver modulates nanoparticle transport, Nat. Nanotechnol. 14 (9) (2019) 874–882.

[46] Y. Kwon, J.H. Yoon, J.H. Ryu, Cyanine-based fluorescent probe for highly selective detection of glutathione in cell cultures and live mouse tissues, J. Am. Chem. Soc. 136 (2014) 5351–5358.

[47] Z. Li, J. Wu, Q. Wang, T. Liang, J. Ge, P. Wang, Z. Liu, A universal strategy to construct lanthanide-doped nanoparticles-based activable NIR-II luminescence probe for bioimaging, iScience 23 (3) (2020), 10096.